ORIGINAL ARTICLE

lajss.org© Latin American Journal of Solids and Structures

www.lajss.org

A Self-adaptive and Lightweight Brace for a Full Cycle of Calf Fracture Rehabilitation

Huan Xue[a,b*], Saiqing Xu[a], Tao Li[a], Xiaojian Peng[a], Chang Guo[a], Ziao Su[c]

[a]Hubei University of Technology, Wuhan, 430068, China. Email: stonemechanics@163.com, 18879695135@163.com, lt1990601@163.com, 17683870483@163.com, gc17807135641@163.com

[b]Hubei Key Laboratory of Modern Manufacturing Quality Engineering, Wuhan, 430068, China.

[c]Wuhan Dehua Testing Engineering Co.,Ltd, Wuhan, 430048, China. Email: 1125161920@qq.com

*Corresponding author

https://doi.org/10.1590/1679-7825/e8484

Abstract

The common treatment for calf fractures is cast immobilization, which limits the movement of the injured area and, causes muscle atrophy and joint stiffness. Wearing a cast for a long time can lead to problems such as itchiness and moist skin. To ameliorate these problems, this study designed a self-adaptive lightweight brace that provides strong patient protection throughout the rehabilitation cycle. The design of the brace is entirely based on the contour of the patient's leg, whereas topological optimization ensures that it meets requirements for lightweightness and air permeability. In the early stages of rehabilitation, the brace provided tight immobilization. During mid-rehabilitation, an automatic airbag filling system inflates in real time to ensure secure immobilization and prevent muscle atrophy or deformity. At the end of rehabilitation, a motorized drive system effectively rehabilitates patient movement. This study verified the effectiveness of the brace self-adaptive system through experimental validation, which involved the recruitment of three volunteers with varying leg circumferences. Volunteers with calf circumference of 34 and 36 cm were tested for reciprocal movement of the leg, and the angle was adjusted and fixed from 99° to 160° and from 104° to 173°, respectively. The automated airbag inflation system was tested on volunteers with calf circumferences of 34 cm. The results of this experiment demonstrated the effective support provided by the proposed brace system throughout the entire calf rehabilitation cycle, indicating its promising application in the medical field.

Keywords

Calf fracture, Full cycle rehabilitation, Self-adaptive lightweight brace, Airbag filling system

Graphical Abstract

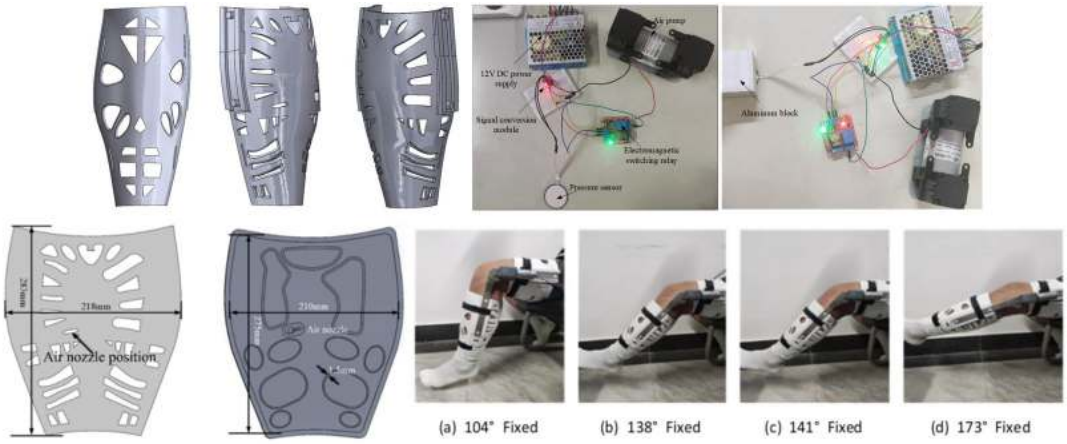

Received December 08, 2024. In revised form February 11, 2025. Accepted March 04, 2025. Available online March 06, 2025.
https://doi.org/10.1590/1679-7825/e8484

Latin American Journal of Solids and Structures. ISSN 1679-7825. Copyright © 2025. This is an Open Access article distributed under the terms of the Creative Commons Attribution License, which permits unrestricted use, distribution, and reproduction in any medium, provided the original work is properly cited.

1 INTRODUCTION

Calf fractures, commonly caused by sports, falls, or accidents, are particularly prevalent among the elderly and adolescents (Liu et al. 2017; Axibal et al.2019). Elderly individuals are prone to osteoporosis and, the developing bones of adolescents are susceptible to external forces (Rizzoli et al. 2010). Immobilization with casts is a common post-surgical requirement; however, it can lead to complications such as skin ulceration and muscle atrophy (Pisecky et al. 2022; Drake and Ritzman 2021). Revolutions in 3D scanning and additive manufacturing have facilitated the production of personalized rehabilitation braces, offering more tailored solutions for patients with calf fractures (Volonghi et al. 2018; Tsiokou et al.2023).

The application of AM in medical rehabilitation has begun with the development of foot and ankle orthoses. Harper et al. (2014) created a foot and ankle orthosis using selective laser sintering (SLS) to aid patients with neuromuscular disorders in improving their walking ability. Subsequently, Pallari Jari et al. (2010) reported orthopedic insoles with SLS for clinical use. However, the limited versatility of orthotics restricts their application to components with similar leg shapes. To address this issue, Scott et al. (2012) designed an adjustable ankle orthosis. Rapid progress in 3D scanning and AM technologies has enabled researchers to personalize custom orthotic designs. Kim and Jeong (2015) proposed a hybrid manufacturing method to fabricate wrist orthoses based on AM and injection molding technology, effectively reducing the cost and time of brace fabrication, and improving patient comfort. Mauren et al. (2017) used 3D printing and 3D scanning to create a personalized and customized brace based on a patient with a distal radius fracture of the left wrist, which made the brace fit the patient's physical characteristics better. Stanciu et al. (2020) utilized 3D scanning technology and AM for forensic applications to obtain a facial replica of a victim by modeling the victim's face, which provides ideas for solving the case. Baronio et al. (2017) used 3D scanning to obtain a model of a patient with hand spasticity and then used AM to create a personalized hand orthosis. The orthosis fits more closely to the contours of the patient's hand and allows for better immobilization. Blaya et al. (2019) implemented personalized fixed splints based on additive manufacturing, industrial digitization, and 3D scanning technology, which fit and fixate the patient's leg well, and are a good solution to problems such as loss of muscle mass and atrophy. The application of AM and 3D scanning technologies has enabled the development of personalized orthotic devices for various body parts. These customized solutions can reduce manufacturing costs and time and improve patient comfort. However, personalized orthoses lack the adaptability to accommodate changes during the rehabilitation process, so a self-adaptive function is needed to ensure the effectiveness of patient rehabilitation.

Compared to traditional casts, self-adaptive braces offer improved breathability and stability, making them essential for addressing the challenges encountered during real-time rehabilitation. Prolonged recovery cycles experienced by fracture patients can result in muscle atrophy and joint stiffness, leading to loose brace fixation and delayed fracture healing. Chen et al. (2017) proposed a self-adaptive oscillator-based method for robot-assisted gait training to help stroke patients complete their daily activities. Wang et al. (2020) designed a self-adaptive ankle-foot exoskeleton based on passive gait, that reduced the flounder myoelectric activity by 72.2% when worn on the human body to assist in walking. Hopkins et al. (2024) designed an ankle-foot orthosis with velocity-self-adaptive stiffness, which provides greater comfort and flexibility for patients with cerebral palsy than traditional fixed-stiffness ankle-foot orthoses. Jradi et al. (2024) proposed a self-adaptive controller applied to a driven ankle foot orthosis, which can provide power to the leg muscles to assist ankle joint movement and help foot drop patients in rehabilitation and walking. Liu et al. (2024) designed a self-adaptive knee orthosis with variable center of rotation to provide rehabilitation assistance for knee flexion and extension movements, improving the efficacy and comfort of knee rehabilitation for patients with knee joint motor dysfunction.

The existing self-adaptive orthotic braces often lack full-cycle rehabilitation capabilities and have limitations in terms of weight and volume. This study proposes a self-adaptive lightweight brace design using flexible sensors and topology optimization to address the limitations of existing braces. The brace conforms to the patient's leg and, provides effective protection and fixation during early rehabilitation. Topology optimization reduces weight and increases breathability, whereas an automatic airbag system ensures a tight fit as the patient experiences muscle atrophy. In addition, a motor-driven system assists in joint rehabilitation and mobility restoration in the final stage. The self-adaptive design offers comprehensive support for patients throughout the entire recovery process.

2 SELF-ADAPTIVE LIGHTWEIGHT BRACE DESIGN PROCESS

The initial step in brace design involves collecting leg contour data from patients. In this study, we utilized an EinScan HX non-contact dual blue light handheld 3D scanner to efficiently capture leg data and ensure precise measurements with exceptional scanning speed and accuracy (Wang et al. 2021; Farhan et al.2021). The acquired leg data were imported into

the Geomagic Design X software for encapsulation, noise reduction, and other processing to obtain the required leg data model. Subsequently, simulations were conducted to generate the NURBS surface (Alejandro et al. 2020; Brujic et al. 2011; Alireza 2021; Gurtej Singh 2021). Owing to the incorporation of an automated airbag filling system into the brace proposed in this study, it is necessary to include an internal liner airbag. Consequently, the constructed surface model of the leg needs to be shifted outward by a certain distance to accommodate the liner airbag and achieve the initial shape of the brace based on the contour of the patient's leg. Subsequently, lightweight design optimization was conducted to enhance the topology of the brace, ultimately resulting in a self-adaptive lightweight brace. The detailed design process is illustrated in Figure 1.

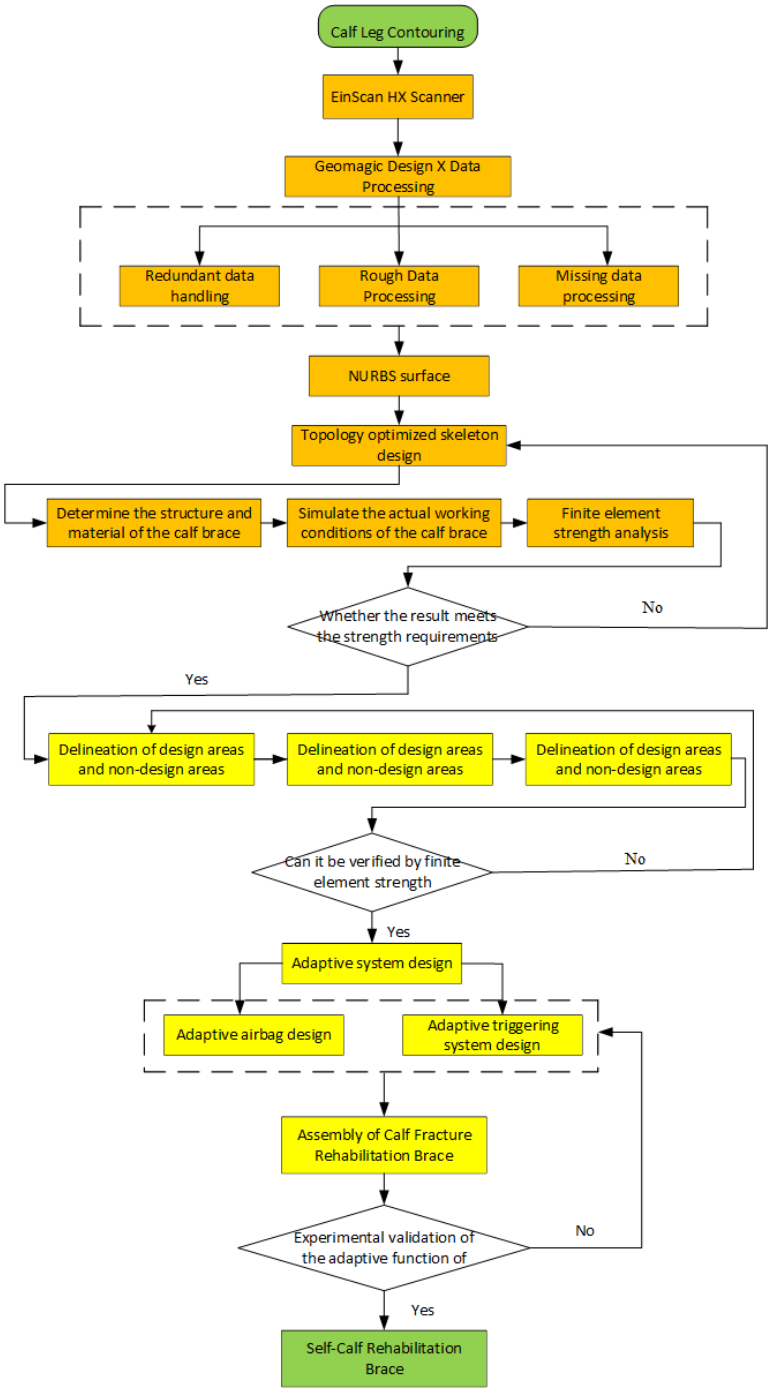

Figure 1 Self-adaptive lightweight brace design process.

3 REVERSE MODELING

This paper presents a personalized brace design that closely conforms to the patient's leg, ensuring early rehabilitation and effectiveness. Data acquisition was performed using the EinScan scanner, as shown in Figure 2 (a),

which displays its physical appearance, and (b) illustrates the data acquisition process. The acquired raw leg data were optimized through Geomagic Design X, a professional tool for reverse engineering and 3D scanning developed by 3D systems. The software facilitates the conversion of scanned data into editable 3D CAD models, enabling efficient creation and modification of intricate engineering designs. Its functionalities include data processing, reconstruction, accuracy verification, and CAD design modeling, making it an indispensable tool for digital design and manufacturing. The optimization process involves addressing redundant, missing, and imprecise information as shown in Figure 3 (a) and (b). Through meticulous optimization of the data process, a refined leg model was successfully obtained as illustrated in Figure 3 (c). The 3D leg model was analyzed and reconstructed using the NURBS surface tool. Subsequently, the face sheet data underwent processing and alignment with the 3D coordinate system before being folded by 3D sketching, as shown in Figure 4 (a). Next, by utilizing the surface release command, the surface data of the leg model were reconstructed to accurately represent its original brace shape based on the calf contour, as illustrated in Figure 4 (b).



Figure 2 Acquisition of leg data.

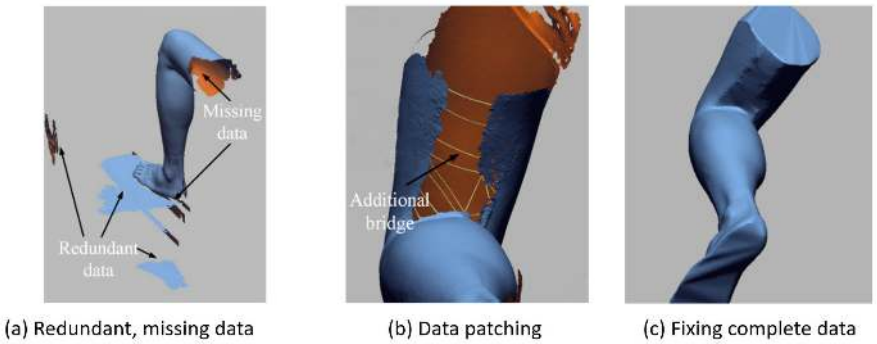

Figure 3 Optimized processing of leg data models.

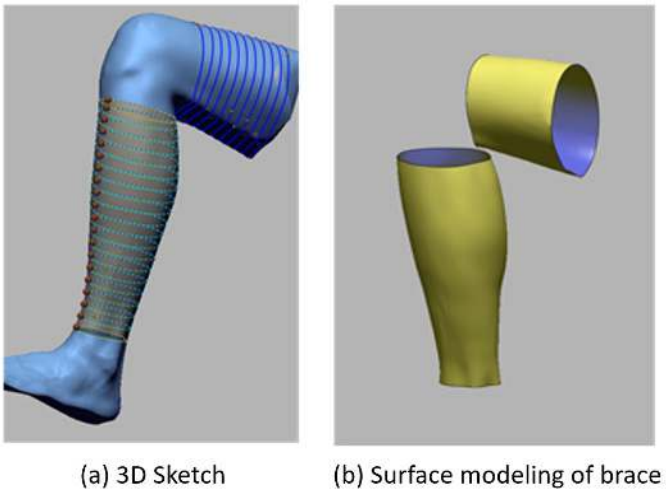

Figure 4 Displacement reconstruction of the leg surface model.

4 REVERSE MODELING

4.1 Lightweight design of brace

The lightweight design of the brace enhances breathability, reducing the risk of skin diseases, and alleviates patient burden during rehabilitation. To achieve lightweight optimization, Hyperworks software was employed for topology optimization in this study. Before optimization, a finite element analysis is conducted to ensure that the brace possesses sufficient structural strength to guarantee wearer safety. To simulate the 10 kg object bumping the brace, the other side of the brace will also be subjected to an opposite force; therefore, in the analysis, the brace is set up before and after the force of the two conditions, the top and bottom of the center of the fixed constraints. These two cases are then superimposed together as a composite case for the finite element strength analysis of the brace. The calf section of the brace was composed of polylactic acid fiber (PLA), with the material parameters listed in Table 1. Figure 5 illustrates both fixed constraints and composite loading conditions.

Table 1. PLA material parameters

Modulus of elasticity (MPa)	Poisson's ratio	Density (g/mm^3)	Yield strength (MPa)
3500	0.35	1.25	65

Brace design is divided into design areas and nondesign areas to optimize the lightweight structure. As shown in Figure 5, the design area includes regions 3 and 5, whereas the nondesign area (regions 1, 2, and 4) constitutes the necessary frame and protective components. The design area allows for a variable topology and material distribution within the specified objectives and constraints.

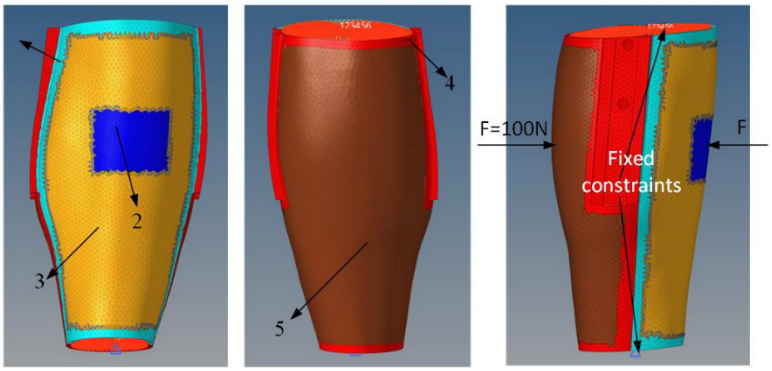

Figure 5 Finite element strength analysis working condition setting.

The results of the finite element analysis are presented in Figures 6 and 7. Figure 6 shows a maximum displacement of 0.156 mm at the fracture point, with a gap of 1 mm between the brace and leg to accommodate the liner. Figure 7 demonstrates that, under an applied pressure of 100 N, the Mises equivalent stress reaches a maximum value of only 2.2 MPa at the fracture location, which is well below the yield strength of the PLA material (65 MPa). These results confirm that the brace design satisfies the required strength specifications.

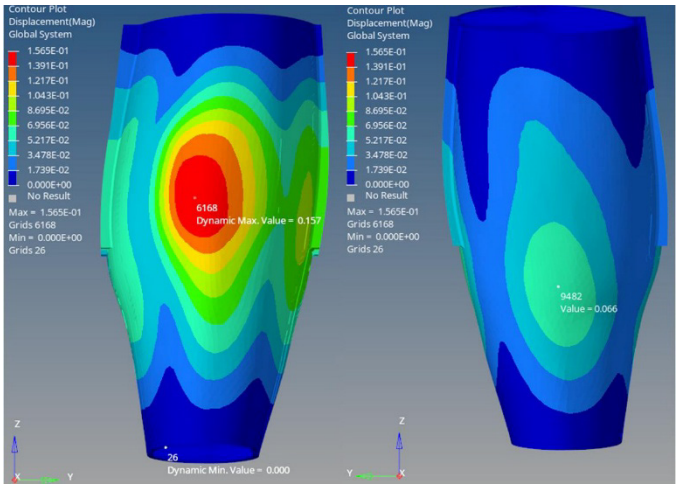

Figure 6 Brace displacement cloud map.

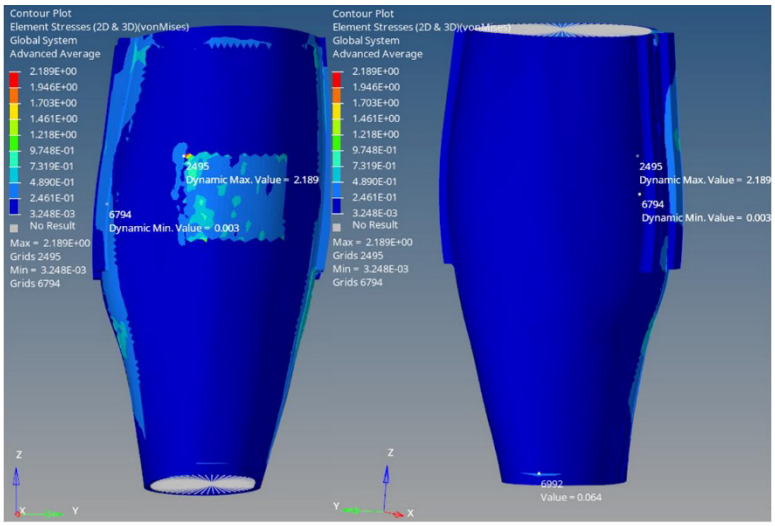

Figure 7 Brace Mises equivalent force cloud map.

After conducting the finite element strength analysis, the subsequent step involves performing topology optimization on the brace. The process of optimization design typically includes three key elements: design variables, constraints, and an objective function. In the case of topology optimization, the design variable is represented by the model cell density. Since this paper utilizes a three-dimensional solid cell model, the chosen methodology for topology optimization is based on variable density (Sigmund 1997). The variable density topology optimization method was first proposed by Rozvany et al. (1995), and then further improved by Bendsøe and Sigmund (1999) and Sigmund (1997), and its two commonly used interpolation methods are Solid Isotropic Microstructure with Penalization (SIMP) and Approximate Model with Reasonable Material Properties (ARMP), respectively. SIMP and approximate models with reasonable material properties. This topology optimization method is based on SIMP interpolation, and the interpolation model is shown in Eqs. (1) and (2):

$$E(\rho) = E_m + x^p (E - E_m) \tag{1}$$

$$E_m = \frac{E}{1000} \tag{2}$$

Where E(ρ) is the elastic modulus of the material after interpolation, and ρ is the relative density of the cell; when ρ is 0, it represents that the cell is empty, and when ρ is 1, it represents that the cell is real; p is the penalization factor, which is generally taken to be 3, and E_m denotes the elastic modulus of the empty cell (the removed cell), and E is the elastic modulus of the material. If E is much larger than E_m, it is negligible and can be written in the form of Eq.(3).

$$E(\rho) = \frac{x^p E}{1000} \tag{3}$$

This design objective is achieved by minimizing the flexibility of the designed brace to meet the strength and stiffness requirements. A linear weighted average method and a compromise planning method are used to transform the multi-case multi-objective optimization into single-case single-objective optimization. The mathematical model for its topology optimization is shown in Eqs. (4) and (5):

$$R(\rho)\min = X^T K X = \left\{ \sum_{j=1}^{m} \varphi_j^p \left[\frac{R(\rho) - (R_j)_{\min}}{(R_j)_{\max} - (R_j)_{\min}} \right]^p \right\}^{\frac{1}{p}} \tag{4}$$

Make:

$$\begin{cases} \sum_{i=1}^{n} \rho_i v_i \le \lambda V \\ KX = F \\ 0 < \rho_{\min} \le \rho_i \le 1 \\ i = 1,2,\ldots,n \end{cases} \tag{5}$$

Where R(ρ) is the overall brace structure flexibility; X_i is the density of unit i calculated by the variable density method; q is the penalty factor; u_i is the column vector displacement matrix of unit i; h_0 is the stiffness matrix of the initial unit of the structure; Vi is the volume of the ith unit; α is the volume ratio. $(R_j)_{max}$ and $(R_j)_{min}$ are the maximum and minimum structural flexibility values for the ith condition, respectively; ϕ_j is the numerical value of the ith condition weight; X is the displacement matrix; K is the initial stiffness matrix; p is the penalty coefficient calculated for the objective function; ρ_i and v_i are the density and volume of the ith cell, respectively; V is the initial design space volume; and F is the column vector of the loading force.

The brace design region underwent topology optimization based on the previous finite element strength analysis. A 100N force was applied to areas 2 and 5, while the constraint objective condition was set as a maximum static displacement of 1mm and volume fraction. The objective function aimed to minimize structural flexibility to maximize stiffness, with the volume fraction constraint representing the percentage change in designable part volume before and after optimization (Borda et al. 2023). The calf brace topology was optimized under volume fraction constraints limited to 20%, 30%, and 40%. As shown in Figure 8, the maximum displacements at the final iteration were -0.209 mm, -0.107 mm, and -0.061 mm respectively, all indicating a reduction compared to pre-optimization values. The highest stresses observed at the last iteration are presented in Figure 9 as follows: under the volume fraction constraints of 20%, 30%, and 40%, they reached magnitudes of 2.6 MPa, 3.01 MPa, and 1.9 MPa respectively along the edges of the brace structure. Notably, for all considered volume fraction limits, stress levels at fracture remained below an acceptable threshold of 1 MPa, thereby satisfying the design requirements set by topology optimization.

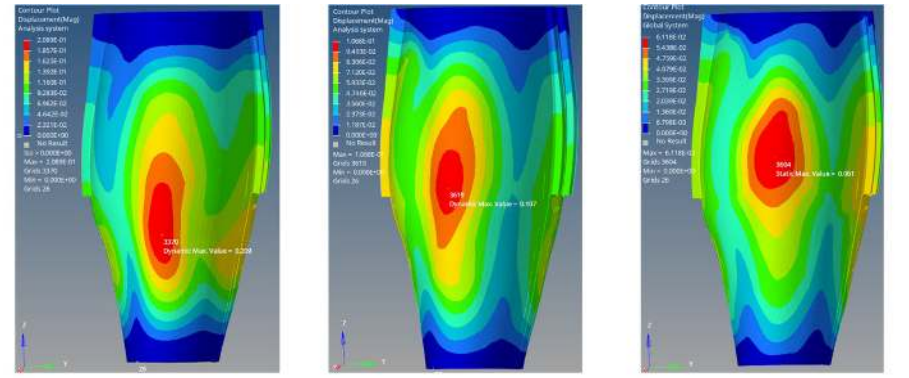

(a) 20% volume fraction bound (b) 30% volume fraction bound (c) 40% volume fraction bound

Figure 8 Displacement of brace after topology optimization.

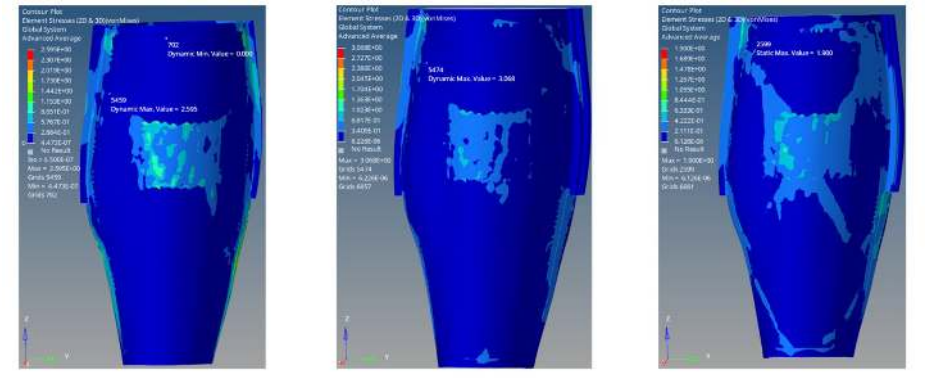

(a) 20% volume fraction bound (b) 30% volume fraction bound (c) 40% volume fraction bound

Figure 9 Stress of the brace after topology optimization.

The flexibility of the objective function decreases and converges to a minimum with increasing iterations, as shown in Figure 10. Initially, the overall flexibility values are highest for the 20% volume fraction constraint, lowest for the 40%, and intermediate for the 30%. As iterations progress, there is a consistent reduction in overall flexibility across all volume fractions; however, it is noteworthy that the 30% constraint exhibits a more significant decreasing trend compared to both the 20% and 40%. The topology optimization results of the calf brace protection device show that in Figure 11, the unit density in the blue area is the lowest, indicating that it can be removed; The unit density in the red area is the highest, suggesting that it must be preserved to ensure strength. To make the protective gear as lightweight and breathable as possible while maintaining its strength, several hollow models with different unit densities were selected for comparison. When the upper limit of volume fraction is 20%, the structural flexibility is maximum, as shown in Figure 12 (a). The hollow model of the left calf guard front cover retains the necessary elements, while the hollow model of the right bottom has a large number of discontinuous elements, which does not meet the requirements. When the upper limit of the volume fraction is 40%, the flexibility of the protective gear is higher than the value under the 30% volume fraction limit, as shown in Figure 12 (c). There are still removable units at the front cover and bottom, and lightweight has not been achieved. When the volume fraction reaches 30%, the density distribution of each element is shown in Figure 12 (b). The hollow model removes unnecessary elements and maintains continuity, achieving minimum flexibility and providing a foundation for lightweight design. Therefore, the unit density distribution with a volume fraction upper limit of 30% was selected as the final hollow model. Figure 13 illustrates the final brace openwork model, which aligns with both the openwork model and topology optimization results.

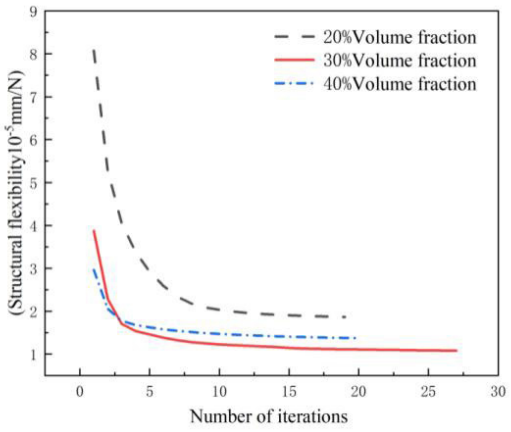

Figure 10 Structural flexibility convergence curves.

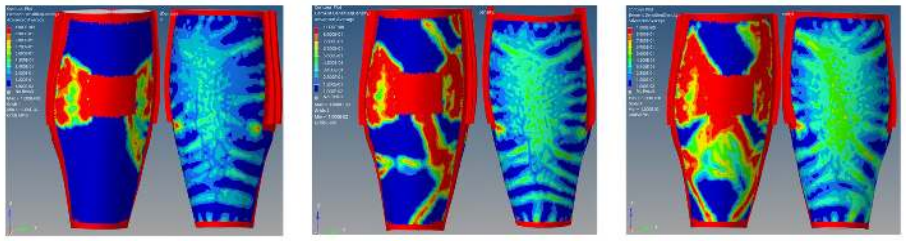

Figure 11 Unit density distribution after topology optimization.

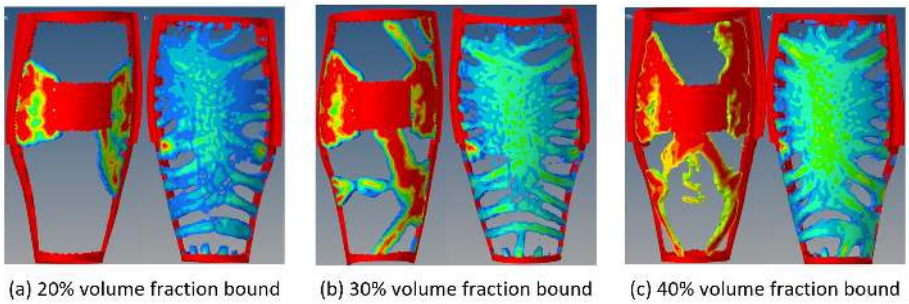

Figure 12 Topological structure of unit density distribution under different volume fraction constraints.



Figure 13 Openwork model.

Due to the incomplete overlap between the hollow design of the calf protector and the topology optimization model, finite element (FEM) strength verification is required. The displacement and stress analysis results are shown in Figures 14 and 15, respectively. The maximum displacement is 0.068mm, far below the installation gap of 1mm; The maximum stress is 0.97 MPa, and the stress at the fracture site is 0.082 MPa, both lower than the yield strength of PLA material at 65 MPa. Therefore, the calf protection device meets the requirements in terms of protection.

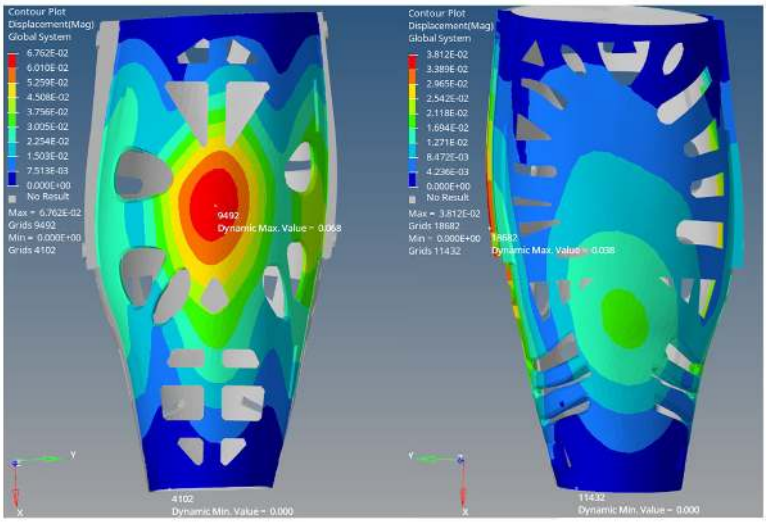

Figure 14 Finite element analysis verifies displacement cloud map.

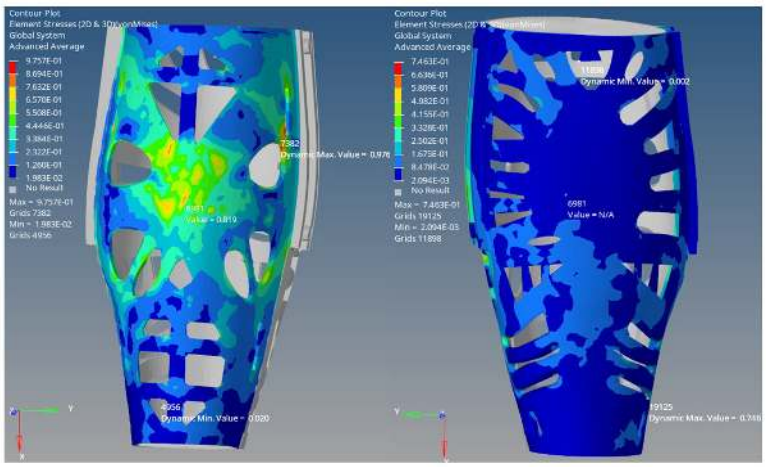

Figure 15 Finite element analysis verifies stress cloud map.

4.2 Design of automatic airbag filling system

The automatic airbag inflation system proposed in this study consists of a thin-film pressure sensor, signal conversion module, electromagnetic switch relay, air pump, airbag, and 12V DC power supply. When the system is activated, the air pump starts to inflate the airbag. The thin-film pressure sensor senses the pressure, and the pressure signal is converted into an electrical signal by the signal converter module, which is then transmitted to the electromagnetic switch relay to close the relay. The normal close contact will break, and the air pump will stop supplying air to the airbag. As shown in Figure 16 (a), the range of the trigger signal can be adjusted by adjusting the comparison threshold, feedback resistor, and size of the sensitivity shim of the linear signal conversion module. The recommended feedback resistance for this linear signal converter is 10 kΩ. Then the comparison threshold is adjusted to the maximum such that the pressure signal is output as completely as possible. The working principle of the signal converter, that is, the core component of the self-adaptive system, is shown in Figure 16 (b), which is mainly composed of a Wheatstone bridge and a comparator. When the thin-film pressure sensor is pressurized, its resistance value Rs will become smaller until R_s is smaller than R_1 when the positive voltage drop of the comparator U+ is larger than the negative voltage drop U-, and at this time, the signal converter sends out an electrical signal to trigger the work of the self-adaptive system. Thin-film pressure sensors have a pressure signal trigger range of 50 g to 2000 g and a sensitivity area of 20 mm in diameter and 400π mm^2 in area.

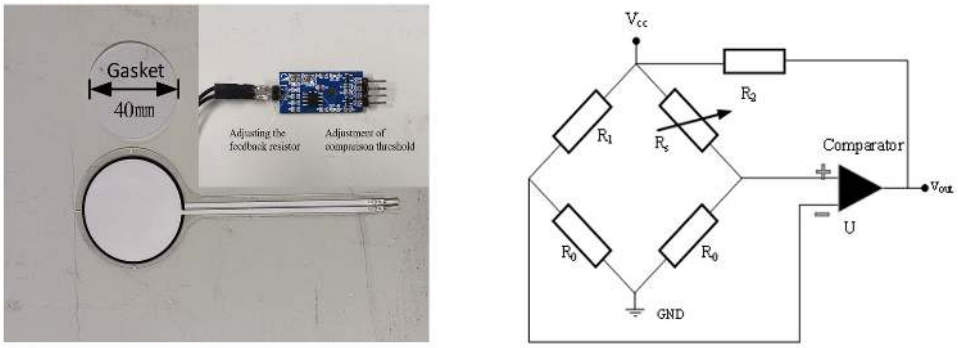

(a) Pressure sensors and signal converters (b) Signal converter working principle

Figure 16 Pressure sensors, signal converters, and their operating principles.

The wiring connections for this system are made on the breadboard by DuPont wire. As depicted in Figure 17, upon the application of a pressure signal to the thin-film pressure sensor, the signal converter transforms it into an electrical signal which is subsequently transmitted to the relay. This results in disconnection and cessation of air supply by the air pump. The airbag inflates and expands to fill the space between the brace and the leg, thus ensuring optimal fixation.

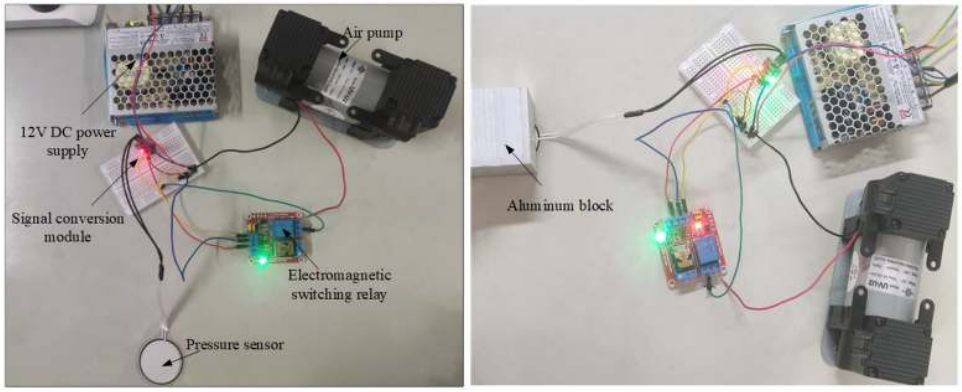

Figure 17 Physical drawing of automatic airbag filling system.

Based on the final brace model, the two components of the calf brace are unfolded in a planar configuration. Considering that external forces do not affect the airbag, the airbag mold is designed by consolidating multiple adjacent openwork holes into a single openwork hole with a regular shape and no sharp corners to ensure structural stability and facilitate fabrication.

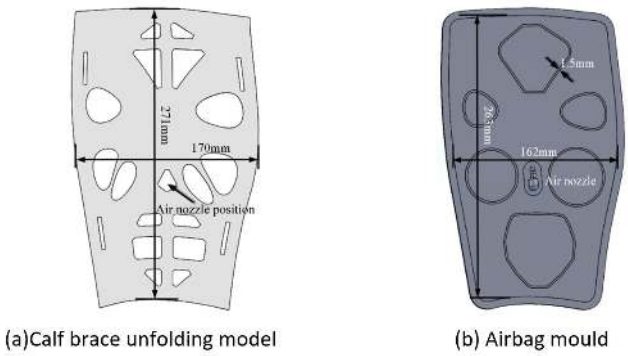

Figure 18 Unfolding model and mold of the airbag of the front cover of the calf brace.

The unfolded model of the calf brace is depicted in Figures 18 and 19 (a), while Figure 19 (b) illustrates the mold of the calf brace lined with the airbag. The front cover and bottom of the guard have respective heights measuring 271 mm and 283 mm, with widths measuring 170 mm and 210 mm respectively. To accommodate edge treatment, a certain distance needs to be allocated for setting aside the mold for the airbag. Consequently, all edges of the deployed calf brace model are inwardly offset by 4 mm.

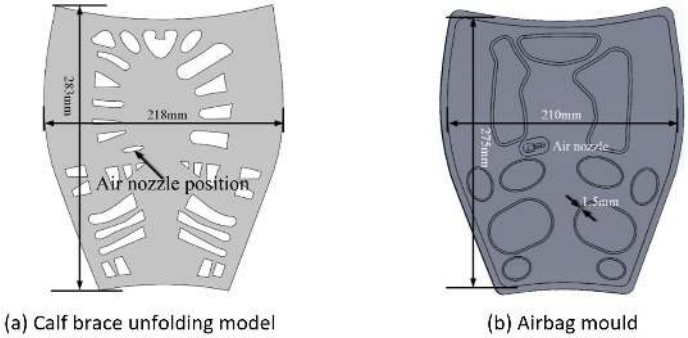

Figure 19 Unfolding model and mold of the airbag at the bottom of the calf brace.

The original brace design shown in Figures 18 (a) and 19 (a) displayed excessive openwork structures with small hole spacing that could potentially result in localized overtightening or overloosening of the airbag, thus impacting fixation stability.To solve this problem, reasonable design adjustments were made to the airbag mold by merging multiple adjacent holes into a single hole and rounding their edges to achieve uniform airbag inflation. As depicted in Figure 20, an ideal position for placing inflation nozzles was identified within the initial skeleton structure without requiring extra holes. Additionally, a skin-friendly composite material composed of TPU and nylon was employed to construct the liner airbag ensuring a secure fit.

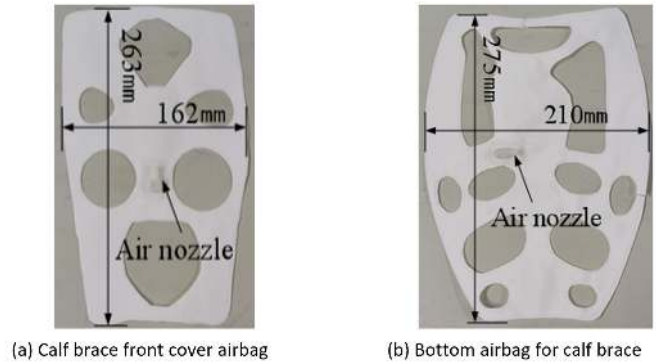

Figure 20 Lined airbag.

4.3 Design of motor-drive systems

Considering that patients at the end of rehabilitation need moderate rehabilitation training. In this paper, a motorized system is designed to drive the patient's leg for reciprocating motion and immobilization. To protect the

patient's safety, the motor-drive system uses 12V DC voltage. The drive motor of the system is a self-locking DC-geared motor, as shown in Figure 21. The motor power P_0 is 8W, the rotational speed n is 3r/min, and its reduction ratio is 1:10. The torque T_0 is calculated as 2.5 N·m by the corresponding formula.

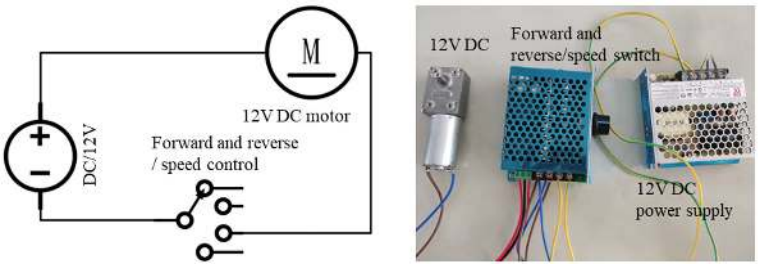

Figure 21 Motor drive system.

In general, the weight of a lower limb in an adult male typically accounts for approximately 18~22% of his total body weight. For instance, considering that the male volunteer in this study weighed 70 kg, based on the uppermost percentage estimation, his leg weight would be around 15.4 kg; however, to ensure safety precautions, a conservative estimate of 10 kg is considered for calf weight. Additionally, Geomagic Design X software offers functionalities to accurately compute facet data attributes such as area, volume and center of gravity. Using its function of calculating the center of gravity, the center of gravity of the triangular faceted data of the calf is calculated to be Q (19.5, -2.5, -235), and the origin of the three-dimensional coordinate system is the center of rotation of the knee joint, so the distance between the origin (0, 0, 0) and the center of gravity of the calf, the distance between the center of gravity of the calf and the center of rotation of the knee joint, L, is 235 mm, as shown in Figure 18. The torque T required to drive the calf around the center of rotation is the torque required to drive the calf, which is calculated to be T=23.5 N·m. Since $10T_0$>T and both lower supports of the brace are fitted with the same type of drive motors, which can provide sufficient power to the calf brace, the system is fully capable of driving the calf to reciprocate on the axis of the center of rotation.

5 EXPERIMENTAL VALIDATION

5.1 Strength analysis

The brace undergoes an overall strength analysis, in which certain geometric features remain unaffected to allow for their simplification. The adjusting support and driving gear are made of 316L stainless steel, while the thigh and calf sections of the brace are composed of PLA material. A weight of 10 kg is assigned to the calf section, and a force of 150 N is applied in the finite element strength analysis to ensure absolute safety. All degrees of freedom at both ends of the thigh are constrained, along with 12456 degrees of freedom at the center of the rotating disk. Only translational degrees of freedom in the Z-axis direction are retained at the center.

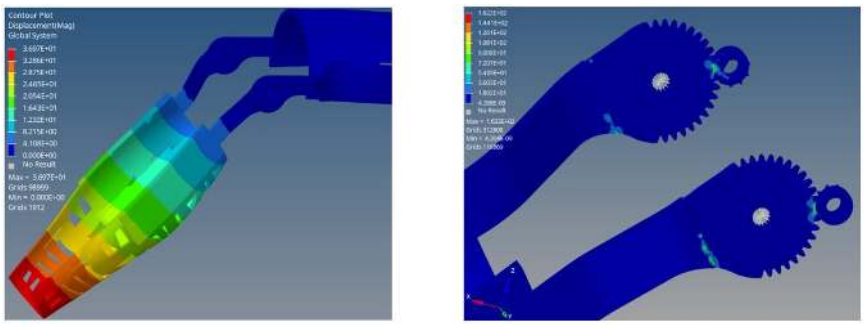

(a) Displacement cloud diagram (b) Stress cloud diagram

Figure 22 Overall strength verification results of the brace.

The results from an overall strength analysis of the brace are presented in Figure 22, which reveals that there is a maximum displacement occurring at its lower end measuring 36.9 mm. Moreover, it can be observed that the rotating large gear experiences a peak Mises equivalent force of up to 162 MPa. Additionally, Figure 23 provides a detailed

depiction of specific stress distribution with a maximum stress value recorded as being 17 MPa at its lower end and reaching up to 24 MPa at its upper end.

The results from an overall strength analysis of the brace are presented in Figure 22, which reveals that there is a maximum displacement occurring at its lower end measuring 36.9 mm. Moreover, it can be observed that the rotating large gear experiences a peak Mises equivalent force of up to 162 MPa. Additionally, Figure 23 provides a detailed depiction of specific stress distribution with a maximum stress value recorded as being 17 MPa at its lower end and reaching up to 24 MPa at its upper end.

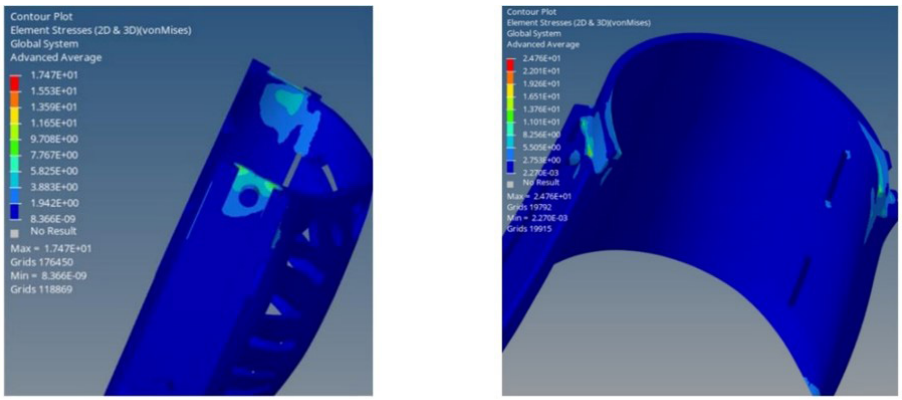

Figure 23 Calf rehabilitation brace upper and lower forces.

The brace is made with PLA for all its components except for the swivel support and gears, which are made from 316L stainless steel. The maximum applied force at both ends of the brace is 24 MPa, while the drive gear experiences a maximum force of 162 MPa. Importantly, both PLA (with a yield strength of 65 MPa) and 316L (with a yield strength of 177 MPa) have values well below their respective material limits to ensure that they meet the required strength criteria.

5.2 Wearing experiment

Three volunteers with varying leg circumferences were recruited to wear the brace in order to evaluate the functionality of the adaptive system. The corresponding data from these volunteer experiments on their legs are presented in Table 2.

Table 2 Test experiment on volunteers with different leg circumferences

Volunteer No. 1	Volunteer No. 2	Volunteer No. 3
Calf circumference 34cm	Calf circumference 36cm	Calf circumference 33cm
Thigh circumference 40cm	Thigh circumference 46cm	Thigh circumference 39cm
Mainly testing the wearing effect of the brace and the motor drive system	The main test of the brace motor drive system	Primary testing of automatic airbag filling systems for braces

The overall assembly effect of the brace is illustrated in Figure 24, while Figures (b) and (c) depict the effects of its wearers, volunteers No. 1 and No. 2, respectively.The specific test steps are as follows: let the volunteer sit on the chair to keep immobilized as much as possible, as shown in Figure 24 (c). Adjustment of the forward and reverse switches allows the calf brace to be fixed at different angles and load testing. As shown in Figure 25, the No. 1 volunteer, who also designed the brace based on his leg model. The wearing experiment is carried out first, and during the adjustment of the angle, every rotation to a certain angle is stopped for a few seconds to test the carrying effect of the brace. The findings demonstrated that the brace effectively supported the leg weight of volunteers at various angles. Equipped with two self-locking DC motors generating a torque of 2×25 N·m, it facilitated reciprocal rehabilitation exercises for the lower limbs effortlessly. During the initial stages of fracture recovery, when comfort is paramount, adjustments to fit the patient's preferred angle are necessary. Given its ability to withstand approximately three times its driving load, thanks to the self-locking DC motor, fixation can be achieved within any flexion range of the knee.



(a) Integral assembly of calf brace (b) Calf circumference 34cm (c) Calf circumference 36cm

Figure 24 Overall assembly of the brace and the effect of volunteers wearing it.



(a) 99° Fixed (b) 135° Fixed (c) 150° Fixed (d) 160° Fixed

Figure 25 Reciprocal exercise and immobilization test in volunteers with a calf circumference of 34 cm.

To further validate the load-bearing capacity and immobilization efficacy of the calf brace, an additional participant (No. 2) with thicker calves was recruited to wear the brace. The testing protocol and procedures were identical to those employed for volunteer No. 1. As depicted in Figure 26, based on the experimental findings, it is evident that the calf brace effectively supports and facilitates reciprocal motion of volunteer No. 2's calf while allowing fixation at any desired angle within its adjustable range.



(a) 104° Fixed (b) 138° Fixed (c) 141° Fixed (d) 173° Fixed

Figure 26 Reciprocal exercise and immobilization test in volunteers with a calf circumference of 36 cm.

After conducting motor-drive system testing on the brace, the automatic airbag filling system is also tested. Due to its design, the brace includes a 1 mm space for installing the liner airbag around the volunteer's leg. When the airbag is not inflated, there is a gap between the brace and the airbag, as shown in Figure 27 (a). When activated, an adaptive system ensures continuous inflation of the airbag using an air pump until it completely fills this gap through a normally closed switch relay. At this point, a thin-film pressure sensor detects and transmits a signal corresponding to the pressure exerted. The signal converter module then converts this pressure signal into an electrical one. Upon receiving said electrical signal, the relay interrupts its normally closed contacts thereby ceasing operation of the air pump. This ensures a tight fit between the leg and the brace at all times.

As volunteers No. 1 and No. 2 wear the brace with a very small gap between it and their leg, it is not possible to effectively test how well the adaptive system works. Therefore, volunteer No. 3, whose legs are more slender, was chosen for the experiment. His thigh and calf circumferences are 39 cm and 33 cm respectively, which can well simulate the calf muscle atrophy that occurs in fracture patients during the rehabilitation process. The gaps between the legs and the brace of the three volunteers after wearing the brace are shown in Figures 27 and 28. Among them, Figures 27 (a) and (b) represent the gap between the legs and the brace of volunteers No. 1 and No. 2, respectively. Volunteer No. 2 has thicker legs, with little to no clearance between the calf and the brace, and the validation of the effectiveness of the working adaptive system is not obvious. The gap between the legs and the brace of the volunteer No. 3 is nearly 10 mm,

which is much larger than the gap between the legs and the brace of the first two volunteers and can be a good test of the working effect of the adaptive system.



(a) Calf circumference 34cm (b) Calf circumference 36cm

Figure 27 Calf circumferences of 34cm and 36cm respectively volunteer gap between calf brace and leg.



Figure 28 Calf circumference 33cm volunteer gap between the calf brace and leg.

When the automatic airbag filling system is activated, the air pump starts to work and the airbag inflates. When the airbag comes into contact with the skin of the calf, the membrane pressure sensor senses the pressure signal and transforms it into an electrical signal through the signal conversion module to be transmitted to the electromagnetic switch relay, which breaks and the air pump stops supplying air. From the partially enlarged images in Figure 29 (a) and (b), it can be seen that the liner airbag bulges and fits tightly to the calf. The liner airbag in this part is also hollowed out because the air permeability of the hollowed-out part has to be maintained. The distance between the hollow part and the calf is sufficient to maintain breathability, thus avoiding the complication of skin diseases.



(a) Back of calf brace (b) Side of calf brace

Figure 29 Work of the automatic airbag filling system.

6 CONCLUSION

The present study focuses on the development of a self-adaptive lightweight brace for the full-cycle rehabilitation of calf fractures, which was structurally designed using 3D scanning and topology optimization techniques, followed by finite element strength analysis. Additionally, a set of self-adaptive systems is incorporated into the brace and tested experimentally. The key advantages can be summarized as follows:

(1) The brace is specifically designed to cater to the rehabilitation requirements of patients with calf fractures, and it can be intelligently adjusted based on individual patient characteristics to provide effective support and protection throughout the entire rehabilitation process.

(2) The contour of the brace is precisely tailored to conform the patient's leg through inverse modeling, ensuring secure fixation and optimizing early-stage rehabilitation outcomes. By employing topology optimization techniques, breathability is enhanced and weight is reduced, thereby alleviating patient burden and mitigating the risk of cutaneous ailment.

(3) Equipped with an automatic airbag filling system and motor-drive system, it solves the problems of muscle atrophy and weakness in the middle and late stages of rehabilitation. This provides a strong guarantee for patient rehabilitation.

Acknowledgements

This study was conducted with the help of the Hubei University of Technology and the Hubei Key Laboratory of Modern Manufacturing Quality Engineering. We express our sincere gratitude to the Key Research and Development Project of Hubei Province (2023BEB043) for providing financial support for this research. Any views, findings, conclusions, or recommendations expressed in this article are similar to those of the author and do not reflect the views of the university, laboratory, or project funding.

Author's Contribuitions: Conceptualization, Huan Xue and Saiqing Xu; Methodology, Huan Xue; Investigation, Huan Xue and Tao Li; Writing - original draft, Huan Xue; Writing - review & editing, Saiqing Xu and Xiaojian Peng; Resources, Ziao Su and Chang Guo; Supervision, Tao Li.

Editor: Marco L. Bittencourt

References

Liu, Y., Liao, Z.W. and Shang, L.(2017). Characteristics of Unilateral Tibial Plateau Fractures Among Adult Patients Hospitalized at an Orthopaedic Trauma Centre in China. Sci. Rep., 7 1-4: 40647.

Axibal, D.P., Mitchell, J.J., Mayo, M.H. (2019). Epidemiology of Anterior Tibial Spine Fractures in Young Patients: a Retrospective Cohort Study of 122 Cases. J. Pediatr. Orthop., 39 2: E87-E90.

Rizzoli, R., Bianchi, M.L., Garabédian, M. (2010). Maximizing Bone Mineral Mass Gain During Growth for the Prevention of Fractures in the Adolescents and the Elderly. Bone 46 2: 294-305.

Pisecky, L., Grossboetzl, G., Gahleitner, M. (2022). Results After Spica Cast Immobilization Following Hip Reconstruction in 95 Cases: Is There a Need For Alternative Techniques?. Arch. Orthop. Trauma Surg., 142 6: 969-977.

Drake, D. F. and Ritzman, T. F. (2021). Cast-Related Complications. Orthop Clin N Am., 52 3: 231-240.

Volonghi, P., Baronio, G., Signoroni, A. (2018). 3D Scanning And Geometry Processing Techniques for Customised Hand Orthotics: An Experimental Assessment. Arch. Orthop. Trauma Surg., 13 2: 105-116.

Tsiokou, V., Papatheodorou, A., Ntenekou, D. (2023). An Integrative Computational Design Workflow and Validation Methodology for 3D-Printed Personalized Orthopedic Devices: Case Study of a Wrist–Hand Orthosis (Who). Processes 11 7: 2204.

Harper, N.G., Russell, E.M, Wilken, J.M. (2014). Selective Laser Sintered Versus Carbon Fiber Passive-Dynamic Ankle-Foot Orthoses: a Comparison of Patient Walking Performance. Journal of Biomechanical Engineering., 136 9: 091001.

Pallari Jari, H.P., Dalgarno, K., James, W. (2010). Mass Customization of Foot Orthoses for Rheumatoid Arthritis Using Selective Laser Sintering. IEEE Trans. Biomed. Eng., 57 7: 1750-1756.

Scott, T., Jari, P., Javier, M. (2012). Embracing Additive Manufacture: Implications for Foot and Ankle Orthosis Design. BMC Musculoskelet. Disord. 13 1: 84.

Kim, H. and Jeong, S. (2015). Case Study: Hybrid Model for The Customized Wrist Orthosis Using 3D Printing. J. Mech. Sci. Tech., 29 12: 5151-5156.

Mauren, S.D.A.,Cristiane S, Marcelo, P.M. (2017). Proposal of custom made wrist orthoses based on 3D modelling and 3D printing. Conference proceedings : ... Annual International Conference of the IEEE Engineering in Medicine and Biology Society. IEEE Engineering in Medicine and Biology Society. Annual Conference., 2017:3789-3792.

Stanciu, N.V., Rosculet, R.T., Fetecau, C. (2020). Forensic Facial Reconstruction Using 3D Printing. Mater Plast., 57 4: 248-257.

Baronio, G., Volonghi, P., Signoroni, A. (2017). Concept and Design of a 3D Printed Support to Assist Hand Scanning for the 463 Realization of Customized Orthosis. Appl. Bionics Biomech., 2017: 8171520.

Blaya, F., San Pedro, P., San Pedro, A.B. (2019). Design of a Functional Splint for Rehabilitation of Achilles Tendon Injury Using Advanced Manufacturing (Am) Techniques. Implementation Study.J. Med. Syst., 43 5: 122.

Chen, G., Qi, P., Guo, Z. (2017). Gait-Event-Based Synchronization Method for Gait Rehabilitation Robots Via a Bioinspired Adaptive Oscillator. IEEE Trans. Biomed., 64 6: 1345-1356.

Wang, X.Y, Guo, S, Qu, B.J. (2020). Design Of a Passive Gait-Based Ankle-Foot Exoskeleton With Self-self-adaptive Capability. Chinese Journal of Mechanical Engineering., 33 5: 212-118.

Hopkins, S., Bowersock, C., Rouse, E.J. (2024). A Quasi-Passive Robotic Ankle Foot Orthosis With Speed-Adaptive Stiffness. IEEE Robot. Automation Lett., 9 2: 1740-1747.

Jradi, R., Rifai, H., Mohammed, S. (2024). Adaptive Active Disturbance Rejection Control of an Actuated Ankle Foot Orthosis for Ankle Movement Assistance. IEEE Robot. Automation Lett., 9 1: 367-374.

Liu, K., Ji, S., Liu, Y. (2024). Design and Optimization of an Adaptive Knee Joint Orthosis for Biomimetic Motion Rehabilitation Assistance. Biomimetics., 9 2: 98.

Wang, R.X., Law, A.C., Garcia, D. (2021). Development of Structured Light 3D-Scanner with High Spatial Resolution and Its Applications for Additive Manufacturing Quality Assurance. Int. J. Adv. Manuf. Technol., 117 3-4: 845-862.

Farhan, M., Wang, J. Z.Z., Bray, P., (2021). Comparison of 3D Scanning Versus Traditional Methods Of Capturing Foot and Ankle Morphology for the Fabrication of Orthoses: a Systematic Review. J. Foot. Ankle Res., 14 1: 2.

Alejandro, P., Naiara, O., Soraya, P. A (2020). Re Methodology to Achieve Accurate Polygon Models and Nurbs Surfaces By 481 Applying Different Data Processing Techniques. Metals., 10 11: 1508

Brujic, D., Ainsworth, I., Ristic, M. (2011) Fast and Accurate Nurbs Fitting for Reverse Engineering. Int. J. Adv. Manuf. Technol. 54: 691-700.

Alireza, H.T. (2021). Generalizations of NURBS and Their Applications in CAGD, and Isogeometric Analysis. Ph.D. Thesis, The University of Wisconsin - Madison, The United States.

Gurtej Singh, C. (2021). Reverse Engineering to Create High Quality Polymer Parts Using Additive Manufacturing. M.S. Thesis, The University of Texas at Arlington, The United States.

Borda, F., La Rosa, A.D., Filice, L. (2023). Environmental Impact of Process Constrained Topology Optimization Design on Automotive Component' Life. Int. J. Mater. Form., 16 5: 48.

Sigmund, O. (1997). On the Design of Compliant Mechanisms Using Topology Optimization. Mech. Struct. Mach. 1997, 25, 493-524.

Rozvany, G.I.N, Bendsoe, M.p., Kirsch, U. (1995). Layout Optimization of Structures. Appl. Mech. Rev. 48 2: 41-119.

Bendsøe, M.P. and Sigmund, O. (1999) Material Interpolation Schemes in Topology Optimization. Arch. Appl. Mech., 69: 635-654.